SDR-implemented passive bistatic SAR system using Sentinel-1 signal and its experiment results

Weike Feng [1], Jean-Michel Friedt [2, *], and Pengcheng Wan [1]

[1] Early Warning and Detection Department, Air Force Engineering University, Xi'an, China.

[2] FEMTO-ST, Time & Frequency department, Besançon, France.

* Correspondence: J-M. Friedt (jmfriedt@femto-st.fr)

Abstract: A fixed-receiver mobile-transmitter passive bistatic synthetic aperture radar (MF-PB-SAR) system, which uses the Sentinel-1 SAR satellite as its noncooperative emitting source, has been developed by using embedded software defined radio (SDR) hardware for high-resolution imaging of the targets in a local area in this study. Firstly, Sentinel-1 and the designed system are introduced. Then, signal model, signal pre-processing methods, and effective target imaging methods are presented. At last, various experiment results of target imaging obtained at different locations are shown to validate the developed system and the proposed methods. It has been found that targets in a range of several kilometers can be well imaged.

1. Introduction

Passive bistatic radar (PBR), which uses noncooperative emitting sources for target illumination, has attracted increasing attentions in the last decades, owing to its unique remote sensing capabilities [1]: 1) no need for frequency allocation; 2) no pollution to the crowded radio frequency environment; 3) relatively low system cost without using dedicated radar transmitter; and 4) target scattering information from a particular bistatic angle. Along with its development, various applications have been realized by PBR, including moving target detection and range-Doppler mapping, synthetic aperture radar (SAR) imaging, air/sea target inverse SAR (ISAR) imaging, displacement estimation, and coherent change detection [2-7].

Among these applications, passive bistatic SAR (PB-SAR) imaging has been used for providing abundant information (e.g., size, shape, and scattering intensity) of stationary targets. Depending on the type of emitting source, the majority of PB-SAR systems can be divided into two categories: fixed-transmitter mobile-receiver PB-SAR (FM-PB-SAR) and mobile-transmitter fixed-receiver bistatic PB-SAR (MF-PB-SAR). In FM-PB-SAR, the emitting source is stationary while the receiver is mobile to get a high cross-range resolution. Different noncooperative signals with a certain bandwidth can be used for FM-PB-SAR [8-11], such as broadcasting digital TV signal (either terrestrial or satellite) and communication WiFi signal. If properly designed, the FM-PB-SAR systems can achieve well-focused image of the targets in a local area. However, in spite of the range resolution determined by the signal bandwidth, the cross-range resolution of FM-PB-SAR is closely related to the receiver motion, which may be restricted in practical implementations (such as the rail length in [8] and [11]). In MF-PB-SAR, the employed noncooperative source is mobile while the receiver is fixed on the ground, thus the system can be more convenient to implement than FM-PB-SAR to get a high cross-range resolution (if no transmitter-receiver synchronization is considered). For example, TerraSAR-X has been used for MF-PB-SAR as the noncooperative emitting source in [12-13] and GNSS signal has been applied for target imaging in [14-15].

45 In recent years, advanced C-band SAR satellites, Sentinel-1 A/B, launched by European Space
46 Agency (ESA) in 2014/2016, have become a burgeoning focus for MF-PB-SAR studies. For example,
47 the COBIS system is presented in [16-17], demonstrating the feasibility of Sentinel-1 signal for MF-
48 PB-SAR imaging. In these works, with specially designed receiver and accessories, timing, frequency,
49 and position synchronization between satellite transmitter and ground receiver has been conducted
50 and the back projection (BP) imaging algorithm has been employed to obtain the image of targets.
51 Besides, via the Terrain Observation with Progressive Scans SAR (TOPSAR) technique, Sentinel-1 can
52 cover three different sub-swaths with a scanning beam, thus the pulse repetition intervals (PRIs) and
53 amplitudes of the received signal pulses will change in a long data-receiving period. In such a case,
54 to improve the cross-range resolution, a multiple-aperture focusing method based on the auto-
55 regressive (AR) model is proposed in [18] and a compressive sensing (CS) based azimuth profile
56 reconstruction method is proposed in [19].

57 Although having been well validated, there are still some problems of current Sentinel-1 based
58 MF-PB-SAR studies: 1) the specialized and exquisite ground receiver makes the system expensive
59 and difficult to implement; 2) the requirement of exact satellite information needs accurate and
60 complicated transmitter-receiver synchronization, reducing the system flexibility; 3) existing target
61 imaging methods, such as the BP and CS based methods presented in [17] and [19], induce high
62 computational costs. Recently, software defined radio (SDR) hardware has been applied to radar
63 applications with an increasing interest, such as the multichannel digital weather radar in [20], the
64 high-range-resolution radar in [21], and the ground-based multiple-input multiple output (MIMO)
65 radar in [22], which shows a low-cost and flexible solution for MF-PB-SAR development because of
66 its reconfigurability and structural universality. Therefore, in this study, to reduce the development
67 cost and improve the system flexibility, we demonstrate the use of commercial-off-the-shelf (COTS)
68 SDR hardware to implement an MF-PB-SAR system using Sentinel-1 as its emitting source, making
69 the system handheld and deployable on remote field areas. Besides, without the requirement of exact
70 satellite information, an effective approach and its high-resolution version realized based on efficient
71 2D CS algorithm are proposed for target imaging with reduced computing complexity.

72 The remainder of this paper is organized as follows. In Section 2, Sentinel-1 and the designed
73 MF-PB-SAR system are introduced. In Section 3, signal model, signal pre-processing methods, and
74 target imaging methods are presented. In Section 4, various experiment results of target imaging at
75 different locations are presented to show the effectiveness of the developed system and the proposed
76 methods. Finally, Section 5 concludes this paper.

2. Sentinel-1 and system overview

78 Sentinel-1 is a set of two SAR satellites at an altitude of 693 km launched by ESA to provide
79 continuous, all-weather, and day-and-night imagery of the Earth surface at C-band. Its resolution,
80 area coverage, and revisit time are more advanced than some others, such as ERS-1/2 and ENVISAT
81 ASAR. The satellites are in a near-polar and sun-synchronous orbit, sharing the same orbit plane with
82 a 180° orbital phasing difference. The repeat cycle of each satellite is 12-day, so the maximal repeat
83 cycle at the equator is 6 days and the revisit rate is greater at higher latitudes, e.g., the Sentinel-1 A/B
84 can be observed at least every three days above 45°N latitude and twice each day at Arctic latitudes.
85 As opposed to dedicated observations as planned for RADARSat or TerraSAR, the continuous
86 monitoring of the Earth by Sentinel-1 allows for accurately predicting its flight time from its orbit
87 period and the observations published on the ESA Copernicus web site [23] with a sub-minute
88 resolution. Knowing the ground station location, its flight geometry can be collected from orbital
89 parameter computation, in our case obtained from the Heavens Above web site [24].

90 To get a large swath width and a moderate resolution at the same time, the interferometric wide
91 swath (IW) mode is used as the default data acquisition mode of Sentinel-1 when scanning the land
92 by using the TOPSAR technique. In IW mode, the satellite transmitted signal is a set of chirp pulses
93 with three different PRIs corresponding to three overlapped sub-swaths on the land, as shown in Fig.
94 1. In such a case, since the satellite moves and periodically steers its antenna beam from sub-swath 1
95 to sub-swath 3, the PRI and amplitude of the IW signal received by a directional antenna fixed on the

96   ground will change along with time, as shown in Fig. 2. It can be seen that three IW signals have
97   different PRIs, i.e., 582.37 μs (IW 1), 688.88 μs (IW 2), and, 593.18 μs (IW 3), as identified from the
98   signal autocorrelation or decoding the level-0 raw data provided by ESA on the Copernicus web site.
99   Futhermore, due to the gains of the satellite antenna and the ground receiving antenna, the ampliudes
100   of different IW signals change greatly and the signal to noise ratio (SNR) is relatively low in some
101   parts. Over sea or remote areas, such as the North Pole, larger swath width and lower resolution in
102   the so-called Extra Wide (EW) measurement mode will be used by Sentinel-1 with different PRIs from
103   the IW measurement mode. The developed system can receive either IW or EW signal by simply
104   changing its corresponding software parameters, making the implementation of the system feasible
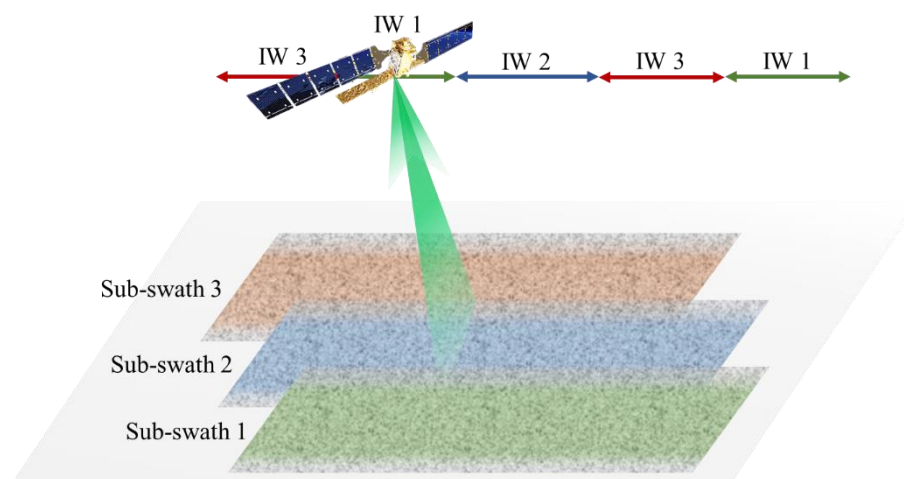105   over most ground covered areas of the Earth.
106

107
108   Fig. 1. The scanning process in the IW mode of Sentinel-1 using the TOPSAR technology, where each
109   sub-swath corresponds to individual IW signal, designated by IW 1, IW 2, and IW 3.
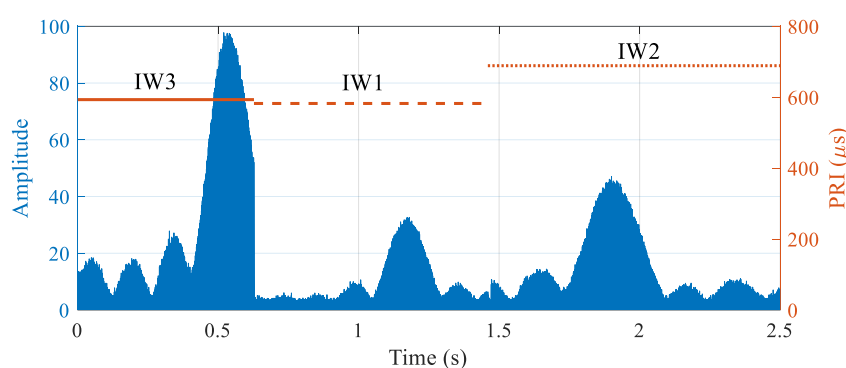110

111
112   Fig. 2. The Sentinel-1 signal received by a directional antenna fixed on the ground: three different
113   PRIs and amplitude differences of these IW signals can be observed.
114

115   The center frequency and bandwidth of the Sentinel-1 signal are 5.405 GHz, corresponding to a
116   wavelength of about 5.55 cm, and up to 100 MHz programmable, respectively. In this study, the
117   bandwidth of the system received signal is limited by the adopted SDR receiver. Considering high-
118   precision data acquisition and transmission in the dual channels of the SDR receiver, the upper signal
119   bandwidth is 30 MHz, providing a bistatic range resolution of 10 m, as shown in Fig. 3, where Fig. 3
120   (a) shows the real part of a received IW 3 signal pulse and Fig. 3 (b) shows its corresponding range
121   ambiguity function.
122   As shown in Fig. 4, the SDR implemented MF-PB-SAR system is mainly composed by two helical
123   antennas (one is used for directly receiving the Sentinel-1 signal, acting as the reference, and another
124   is used for receiving the target reflections in the observed scene, named as surveillance), a SDR
125   receiver (Ettus B210), a single board Raspberry Pi 4 (RPi 4) used to collect and store the data, and a

126 host computer for signal processing and result displaying. Detailed information of these components
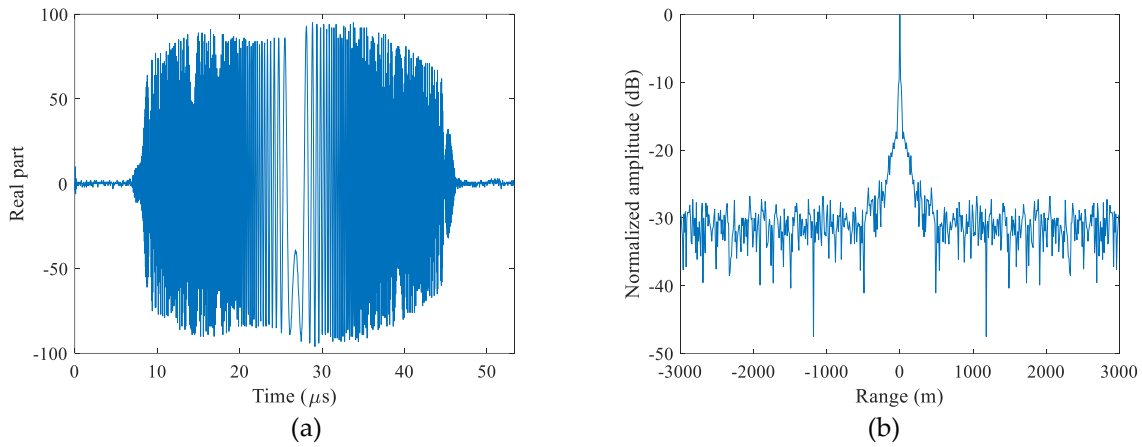127 is given as follows.
128

129
130 (a) (b)
131 Fig. 3. (a) Real part of a received signal pulse (IW 3) and (b) its range ambiguity function, showing a
132 bistatic range resolution of 10 m with the SDR receiver setup limited to a 30 MHz bandwidth.
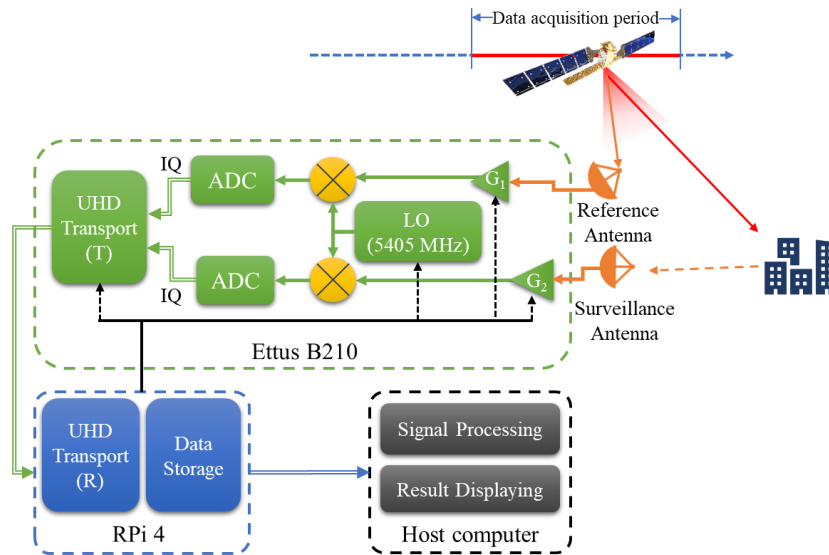133

134
135 Fig. 4. The general structure of the developed MF-PB-SAR system, including one SDR receiver (Ettus
136 B210), a host computer, a RPi 4, and two antennas (reference and surveillance antennas).
137
138 **(1) Antennas.** The helical antennas are designed according to [25] by winding 4 turns of
139 enameled copper wire around a 15 mm hollow teflon tube, providing a frequency band from 4.8 to
140 8.5 GHz, including the Sentinel-1 signal band. The low antenna gain design of 5 dB is selected for a
141 wide beam to observe a broad imaging scene. The reference antenna is set at an angle matching the
142 satellite elevation during its pass and the surveillance antenna is set pointing to the targets in the
143 observation scene.
144 **(2) SDR Receiver.** The 70 MHz–6 GHz COTS Ettus B210 dual channel SDR hardware is chosen
145 as the receiver of the developed MF-PB-SAR system due to its high performance and low cost. Two
146 receiving channels share a local oscillator (LO), setting as 5405 MHz, and the parameters (e.g., gain
147 and offset) of each channel are adjusted according to the practical condition. As mentioned above,
148 the data sampling frequency of Ettus B210 is set as 30 MS/s considering the dual channel high-
149 precision data acquisition and transmission.
150 **(3) RPi 4:** The single board computer RPi 4 fitted with a USB 3.0 port collects the data from the
151 B210 and stores them in its RAM. Data collection duration and communication speed are maximized
152 by reducing the sample resolution to a single byte/sample. Hence, at a rate of 30 MS/s, the complex

153 dual channel sample will require 7.2 GB/minute. The 8 GB RAM version of the RPi4 can hence hold
154 1-minute worth of data or twice the pass duration of the satellite, allowing sample flexibility in data
155 acquisition starting time.

156 **(4) Host computer:** Once the 7.2 GB of data have been collected in RPi 4, they are transferred to
157 the host computer. Signal pre-process and process, as will be introduced in the next Section, will be
158 then conducted and the target imaging results will be finally displayed.

159 The overall working flow of the developed MF-PB-SAR system can be summarized as:

160 1) The reference antenna orientation is set to ensure maximum reception of the direct satellite
161 signal on the foundation of its relative position to Sentinel 1, where the scheduled pass geometry of
162 the satellite is queried in public information, such as the Heavens Above web site. The surveillance
163 antenna is facing the targets, and, to reduce the direct-path interference (DPI) in the surveillance
164 channel, the surveillance antenna is set properly to make the satellite within its side lobe during the
165 measurement.

166 2) The time window for data acquisition is determined from past datasets made available on the
167 ESA Copernicus web site, whose file name includes the beginning and ending of the data sampling
168 with one second resolution. While a horizon-to-horizon satellite pass lasts 9 minutes, a given area is
169 only illuminated for a few seconds. As introduced before, the satellite repeats its pattern over a period
170 of 12 days. By searching the pattern over the scheduled site in the previous public raw data, the future
171 accurate acquisition time within several seconds can be determined.

172 3) The signal of two channels will be collected and converted into complex format by Ettus B210
173 and transmitted to RPi 4. RPi 4 stores the data in its RAM and later transfer them to the host computer,
174 which will finally analyze and process the data by the proposed methods.

175 With a current consumption of 1.55 A at 5 V supply when running at full speed in performance
176 mode (1.5 GHz) as needed to collect and store the data, the setup will allow for collecting up to 85
177 datasets autonomously on a single 2200 mAh battery pack as used in the system.

178 **3. Signal model and processing methods**

179 *3.1. Signal modeling and pre-processing*

180 In this sub-Section, the signal modeling and pre-processing methods for the developed MF-PB-
181 SAR system are presented.

182 Firstly, assume the received reference signal and surveillance signal are expressed as $s_{ref}(n)$
183 and $s_{ref}(n)$ in the discrete time domain, respectively, with $n = f_s t$, t as time, and f_s as the system
184 sampling frequency. Since the SNR of the received signals will change along with time, the first signal
185 pre-processing step we conducted is to select a specific IW (EW) signal fragment and then determine
186 its corresponding PRI for the following process. Here, we select the IW (EW) signal fragment sampled
187 when the satellite just flies above and its beam just steers to the experiment site. As shown in Fig. 2,
188 the corresponding IW (EW) signal fragment can be selected according to the amplitude of the
189 received reference signal. If the satellite is above the experiment site, the SNR of the reference signal
190 will be the highest. Thus, given an amplitude threshold χ, set according to practical conditions, the
191 starting and ending points of the selected IW (EW) signal fragment can be obtained as n_s and n_e
192 with $s_{ref}(n_s) \geq \chi$ and $s_{ref}(n_e) \geq \chi$. We note that, out of the collected data samples, the selected signal
193 fragment will last typically a few hundred milliseconds at most.

194 For the selected signal fragment, a 2D reference signal matrix can be formed by

$$S_{ref} = [s_{ref}^1, s_{ref}^2, ..., s_{ref}^P] \in C^{N_r \times P} \tag{1}$$

196 where N_r denotes the number of selected sampling points in each PRI, determining the system
197 maximal detection range, P denotes the number of selected PRIs, determined by n_s and n_e as
198 $P = \lfloor (n_e - n_s)/N_0 \rfloor$, and $s_{ref}^P (p = 1, 2, ..., P)$ can be expressed as

$$s_{ref}^P = [s_{ref}(n_s + (p-1)N_0), s_{ref}(n_s + (p-1)N_0 + 1), ..., s_{ref}(n_s + (p-1)N_0 + N_r - 1)]^T \in C^{N_r \times 1} \tag{2}$$

200 with $(\cdot)^{\mathrm{T}}$ as matrix transpose, $N_0 = \lfloor f_s T \rfloor \geq N_r$ as the number of sampling points corresponding to
201 the PRI T, depended on the IW or EW, and $\lfloor \cdot \rfloor$ as the floor function.
202 Only when the correct PRI is adopted for the selected signal fragment, the signal matrix in (1)
203 can be used for following process. Besides, to ensure the signal matrix in (1) contains all samples of
204 each IW (EW) signal pulse, the starting and ending points n_s and n_e should be fine-tuned after the
205 initial detection. For example, for the reference signal shown in Fig. 2 with an amplitude threshold of
206 $\chi = 60$, the obtained signal matrix is presented in Fig. 5 with the number of sampling points in each
207 PRI as $N_r = 2401$, corresponding to a maximal detection range of 24 km given $f_s = 30$ MS/s. It can
208 be seen from Fig. 5 that the IW 3 signal fragment with a PRI of 593.18 μs is selected with $P = 251$
209 PRIs, and, in order to contain all the samples of each pulse, some reserved sample points are included
210 at the beginning of each PRI. If an incorrect PRI is used, the signal matrix will not be well aligned, as
211 shown in Fig. 5 (b) and (c).
212

213
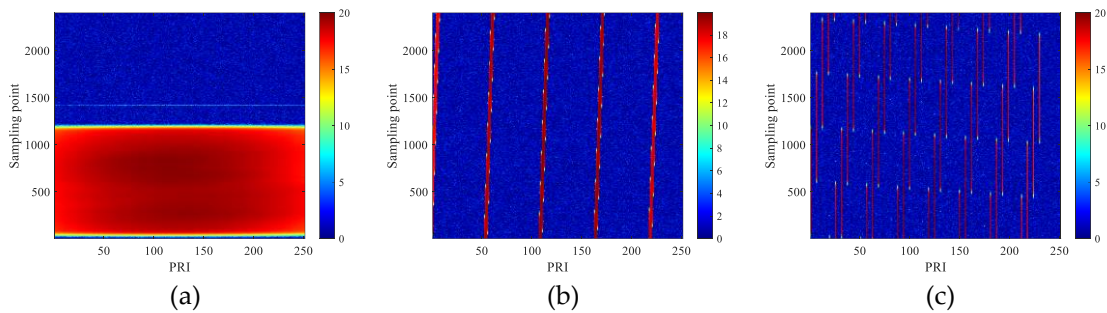214   (a)   (b)   (c)
215 Fig. 5. The obtained 2D reference signal matrices with (a) PRI = 593.18 μs (IW 3), (b) PRI = 582.37 μs
216 (IW 1), and (c) PRI = 688.88 μs (IW 2).
217

218 Similarly, a 2D surveillance signal matrix can also be generated, expressed as
219
$$\mathbf{S}_{sur} = [\mathbf{s}_{sur}^1, \mathbf{s}_{sur}^2, ..., \mathbf{s}_{sur}^P] \in C^{N_r \times P} \tag{3}$$

220 where
221
$$\mathbf{s}_{sur}^p = [s_{sur}(n_s + (p-1)N_0), s_{sur}(n_s + (p-1)N_0 + 1), ..., s_{sur}(n_s + (p-1)N_0 + N_r - 1)]^{\mathrm{T}} \in C^{N_r \times 1} \tag{4}$$

222 In this study, as shown in Fig. 6, we assume the ground target is located at (x, y) with the height
223 of 0, the reference and surveillance antennas are collocated at $(0,0,0)$, and, at the p-th PRI in the
224 selected IW (EW) signal fragment, the satellite is at $(-H \cot \varphi, y_{sat}^p, H)$ with H as its height (693 km),
225 φ as its incident angle (depending on the satellite beam), and the y axis as its moving direction.
226 For imaging process, a plane (i.e., α-o-β) is formed by the satellite path (i.e., the dotted red line
227 in Fig. 6) and the antenna position. On the α-o-β plane, the antennas are at $(0,0)$, the target is at (α, β),
228 and the p-th satellite position is $(\alpha_{sat}^p, \beta_{sat})$ with $\alpha_{sat}^p = y_{sat}^p$ and $\beta_{sat} = -H / \sin \varphi$, where $\alpha_{sat}^p = \alpha_{sat}^c$
229 $+[p-1-(P-1)/2]d$, $d = vT$, and v denotes the linear speed of the satellite, which is estimated to
230 be 7.49 km/s based on the satellite altitude and the orbit period 98.684 minutes. The center satellite
231 position α_{sat}^c will be 0 if the IW (EW) signal fragment is ideally selected.
232 Assuming the satellite transmitted signal at the p-th PRI in the selected IW (EW) signal fragment
233 is $g_0^p(\tau)$ in the continuous time domain with $\tau \in [0, T]$, the received signals by the reference and
234 surveillance antennas can be expressed as
235
$$g_{ref}^p(\tau) = A^p g_0^p(\tau - \tau_{ref}^p), \quad g_{sur}^p(\tau) = \sigma(\alpha, \beta) g_0^p[\tau - \tau_{sat}^p(\alpha, \beta) - \tau_{sur}(\alpha, \beta)] + g_{dpi}^p(\tau) \tag{5}$$

236 where A^p denotes the amplitude of the reference signal in the p-th PRI, affected by the gains of
237 satellite and reference antennas, $\sigma(\alpha, \beta)$ denotes the target reflection coefficient, $g_{dpi}^p(\tau)$ denotes
238 the DPI signal (i.e., the satellite signal received directly by the surveillance antenna), and
239
$$\tau_{ref}^p = \sqrt{(\alpha_{sat}^p)^2 + \beta_{sat}^2} / c, \quad \tau_{sur}(\alpha, \beta) = \sqrt{\alpha^2 + \beta^2} / c, \quad \tau_{sat}^p(\alpha, \beta) = \sqrt{(\alpha_{sat}^p - \alpha)^2 + (\beta_{sat} - \beta)^2} / c \tag{6}$$

240 denote the delays from the satellite to the reference antenna, from the target to the surveillance
241 antenna, and from the satellite to the target, with c as the speed of light.

242 Based on (5) and according to the signal matrix formation procedure, the n_r-th ($n_r = 1, 2, ..., N_r$)
243 elements of s_{ref}^p and s_{sur}^p can be expressed as

$$s_{ref}^p(n_r) = g_{ref}^p\{\tau = (n_r - 1 - n^p)/f_s + \tau_{ref}^p\}, \ s_{sur}^p(n_r) = g_{sur}^p\{\tau = (n_r - 1 - n^p)/f_s + \tau_{ref}^p\} \tag{7}$$

245 where n^p denotes the number of reserved sampling points as shown in Fig. 5 (a).
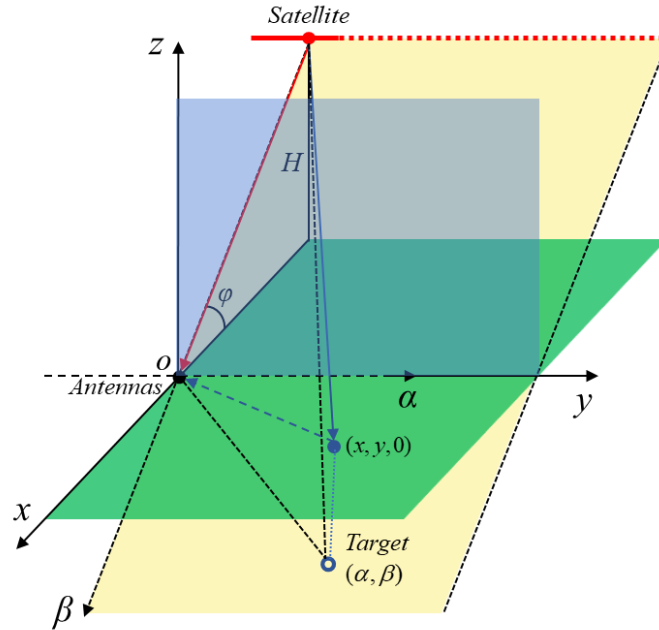
246

247
248 Fig. 6. Imaging geometry of the developed SDR MF-PB-SAR system with the satellite height H = 693
249 km and the incident angle φ of the satellite obtained from the Heavens Above web site. The target in
250 the *x-o-y* plane has been projected on the *α-o-β* plane for imaging process.

251

252 Since it is always much stronger than the target reflections, the DPI component in s_{sur}^p will have
253 seriously negative influence on the imaging performance. To solve this problem, the second signal
254 pre-processing step we conducted is to suppress the DPI while keeping the target reflections. In this
255 study, the LS-based method [11] is used to do so, giving

$$s_{sur}^p \leftarrow s_{sur}^p - U_p(U_p^H U_p)^{-1} U_p^H s_{sur}^p \tag{8}$$

257 where $(\cdot)^H$ denotes conjugate transpose, $(\cdot)^{-1}$ denotes matrix inverse, and U_p is constructed by the
258 delayed copies of s_{ref}^p, expressed as

$$U_p = [u_p^1, u_p^2, ..., u_p^L] \in C^{N_r \times L} \tag{9}$$

260 where

$$u_p^l = [s_{ref}(n_s + (p-1)N_0 - l), s_{ref}(n_s + (p-1)N_0 + 1 - l), ..., s_{ref}(n_s + (p-1)N_0 + N_r - 1 - l)]^T \in C^{N_r \times 1} \tag{10}$$

262 with $l = 1, 2, ..., L$ as the discrete time delays used to properly model the DPI.

263 Furthermore, in order to reduce the influence of amplitude difference of the signals in different
264 PRIs on target imaging, the last signal pre-processing we conducted in this study is to proportionally
265 estimate $A = [A^1, A^2, ..., A^P] \in R^{1 \times P}$, based on which the received reference signals will be compensated.
266 It should be noted that, because the target reflection signals are much smaller and thus more affected
267 by noise, amplitude differences of the surveillance signals in different PRIs will not be compensated
268 in order to avoid increasing the noise level.

269 To proportionally estimate A, the amplitude maximum of the reference signal in each PRI is
270 calculated firstly to get

$$|S_{ref}|_{max} = [|s_{ref}^1|_{max}, |s_{ref}^2|_{max}, ..., |s_{ref}^P|_{max}] \in R^{1 \times P} \tag{11}$$

272   Then, a cubic polynomial curve fitting method is used to get the estimation of A^p, expressed as

273
$$|S_{ref}|_{\max}(p) \simeq \sum_{i=1}^{3} a_i p^i \rightarrow A^p = \sum_{i=1}^{3} a_i p^i \tag{12}$$

274   At last, the received reference signals can be compensated by

275
$$S_{ref} \leftarrow [s_{ref}^1 / A^1, s_{ref}^2 / A^2, ..., s_{ref}^P / A^P] \tag{13}$$

276   Based on (8) and (13), 2D reference and surveillance signal matrices can be obtained, establishing
277 the signal model used in this study and laying the foundation for the following imaging process.

3.2. Effective imaging methods

279   In this sub-Section, effective target imaging methods are proposed for the developed system.
280 Firstly, for the p-th PRI of the obtained signal matrices, the reference and surveillance signal vectors
281 s_{ref}^p and s_{sur}^p are transformed to the discrete frequency domain, giving

282
$$\begin{cases} s_{ref}^p(f_{n_r}) = G_0^p(f_{n_r})\exp(-j2\pi f_{n_r}n^p/f_s) \\ s_{sur}^p(f_{n_r}) = \sigma(\alpha,\beta)G_0^p(f_{n_r})\exp(-j2\pi f_{n_r}n^p/f_s)\exp\{j2\pi f_{n_r}[\tau_{ref}^p - \tau_{sat}^p(\alpha,\beta) - \tau_{sur}(\alpha,\beta)]\} \end{cases} \tag{14}$$

283 where $f_{n_r} = f_c + [n_r - 1 - (N_r - 1)/2]f_s/N_r$ denotes the n_r-th frequency ($n_r = 1, 2, ..., N_r$), f_c denotes
284 the center frequency, and $G_0^p(f_{n_r})$ denotes the spectrum of the transmitted signal $g_0^p(\tau)$.

285   Then, a signal vector in the discrete frequency domain can be obtained by combing the reference
286 and surveillance vectors, as

287
$$s^p(f_{n_r}) = s_{sur}^p(f_{n_r})[s_{ref}^p(f_{n_r})]^* = \sigma(\alpha,\beta)\exp\{-j2\pi f_{n_r}[\tau_{sat}^p(\alpha,\beta) - \tau_{ref}^p + \tau_{sur}(\alpha,\beta)]\} \tag{15}$$

288 where $[\cdot]^*$ denotes conjugate and, since the signal spectrum $G_0^p(f_{n_r})$ is flat, we set $|G_0^p(f_{n_r})|^2 = 1$
289 for simplification in (15).

290   As the satellite is far from the antennas and the targets, the following approximations can be
291 used based on the second-order Taylor expansions

292
$$\tau_{ref}^p \simeq [-\beta_{sat} - (\alpha_{sat}^p)^2/(2\beta_{sat})]/c, \quad \tau_{sat}^p(\alpha,\beta) \simeq [(\beta - \beta_{sat}) - (\alpha_{sat}^p - \alpha)^2/(2\beta_{sat} - 2\beta)]/c \tag{16}$$

293 and thus

294
$$\tau_{sat}^p(\alpha,\beta) - \tau_{ref}^p \simeq [\beta + (\alpha_{sat}^p\alpha - \alpha^2/2)/(\beta_{sat} - \beta)]/c \tag{17}$$

295 where the term related to the square of α_{sat}^p is ignored considering it is relatively much smaller.
296 According to (17), the signal vector given in (15) can be approximated by

297
$$s^p(f_{n_r}) \simeq \sigma(\alpha,\beta)\exp[-j2\pi f_{n_r}(\beta_I/c + \alpha_{sat}^p\alpha_I/c)] \tag{18}$$

298 where $\beta_I = (\alpha^2 + \beta^2)^{1/2} + \beta - \alpha^2/(\beta_{sat} - \beta)/2$ and $\alpha_I = \alpha/(\beta_{sat} - \beta)$.

299   Furthermore, as the signal bandwidth is much smaller than the signal center frequency, the
300 following approximation can be used

301
$$\exp\{-j2\pi f_{n_r}\alpha_{sat}^p\alpha/c\} \simeq \exp\{-j2\pi\alpha_{sat}^p\alpha_I/\lambda_c\} \tag{19}$$

302 where λ_c denotes the signal wavelength corresponding to the center frequency f_c.

303   Therefore, (18) can be approximated by

304
$$s^p(f_{n_r}) \simeq \sigma(\alpha,\beta)\exp[-j2\pi f_{n_r}\beta_I/c]\exp[-j2\pi\alpha_{sat}^p\alpha_I/\lambda_c] \tag{20}$$

305   For a local imaging scene, the phase difference between (20) and (15) is always small. For example,
306 given $\beta_{sat} = -1000\,km$, satellite moving length as 1350 m (corresponding to $P = 301$ and $d = 4.5\,m$,
307 longer than those used in the field experiments), center satellite position as $\alpha_{sat}^c = 0$, and an imaging
308 scene with $\alpha \in [-5\,km, 5\,km]$ and $\beta \in [0, 10\,km]$, which is the maximal imaging size in the various
309 experiments conducted in different locations by the developed system, the maximal phase difference
310 between (20) and (15) for all satellite positions and all frequencies of different targets in the imaging
311 scene is shown in Fig. 7 (a). Besides, as the center satellite position will deviate from 0 if the IW (EW)
312 signal fragment is not ideally selected, Fig. 7 (b) shows the maximal phase difference between (20) and
313 (15) of all the targets in the imaging scene with respect to $\alpha_{sat}^c \in [-100\,m, 100\,m]$. It can be learned from

314   Fig. 7 that, for the given parameters, the phase difference between (20) and (15) is always smaller than
315    $\pi/2$, verifying the feasibility of applying (20) for the following target imaging process [26-27].
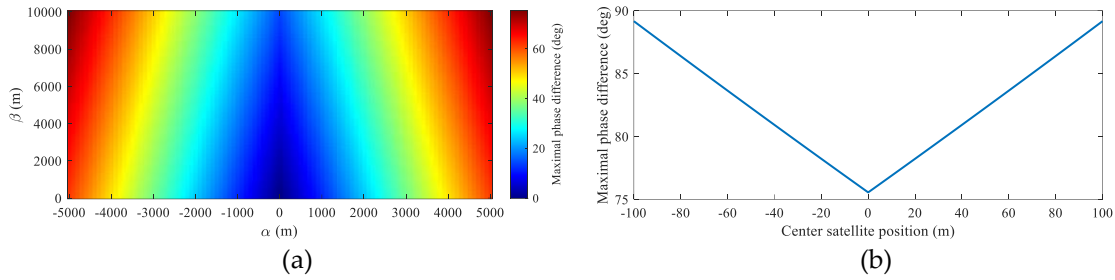
316
317   (a)   (b)

318   Fig. 7. (a) Maximal phase difference for all satellite positions and all frequencies of different targets in
319   the imaging scene with the satellite center position as 0 and (b) maximal phase difference of the
320   imaging scene with different satellite center positions.
321

322   It can be observed from (20) that its exponential terms form the kernels of a 2D Fourier transform
323   (FT) with respect to α_I and β_I. Therefore, 2D inverse fast FT (IFFT) can be used to get a focused
324   image as

325
$$\boldsymbol{\Sigma}_{LR} = \boldsymbol{F}_1^H \boldsymbol{S} \boldsymbol{F}_2^* \in C^{O \times L} \tag{21}$$

326   where $\boldsymbol{S} = [\boldsymbol{s}^1, \boldsymbol{s}^2, ..., \boldsymbol{s}^P] \in C^{N_r \times P}$, $\boldsymbol{F}_1 \in C^{N_r \times O}$ and $\boldsymbol{F}_2 \in C^{P \times L}$ denote the FT matrices, given by

327
$$\boldsymbol{F}_1 = \exp[-j2\pi \boldsymbol{f}_r \boldsymbol{\beta}_I^T / c], \quad \boldsymbol{F}_2 = \exp[-j2\pi \boldsymbol{\alpha}_{sat} \boldsymbol{\alpha}_I^T / \lambda_c] \tag{22}$$

328   with $\boldsymbol{f}_r = [f_1, f_2, ..., f_{N_r}]^T - f_c$, $\boldsymbol{\alpha}_{sat} = [\alpha_{sat}^1, \alpha_{sat}^2, ..., \alpha_{sat}^P]^T - \alpha_{sat}^c$, $\boldsymbol{\beta}_I \in R^{1 \times O}$ and $\boldsymbol{\alpha}_I \in C^{1 \times L}$ set according
329   to the imaging scene size.
330   Based on (20), it can be derived that the $[o, l]$-th element of $\boldsymbol{\Sigma}_{LR}$ can be expressed as

331
$$\boldsymbol{\Sigma}_{LR}(\beta_I^o, \alpha_I^l) = \sigma(\alpha, \beta) e^{-j2\pi(\beta_I - \beta_I^o)/\lambda_c} e^{-j2\pi\alpha_{sat}^c(\alpha_I - \alpha_I^l)/\lambda_c} \mathrm{sinc}[B_r(\beta_I - \beta_I^o)/c] \mathrm{sinc}[B_a(\alpha_I - \alpha_I^l)/\lambda_c] \tag{23}$$

332   where $B_r = f_s$ and $B_a = Pd$ denotes the signal bandwidth in the β_I and α_I directions, respectively.
333   In spite of its efficiency, the imaging process based 2D IFFT limits the imaging resolution and
334   generates high-level imaging sidelobes. To suppress sidelobes and improve resolution, the sparsity
335   of the scene can be exploited based on the CS theory [28-29]. In this study, the following minimization
336   problem is established to achieve a high-resolution target image

337
$$\boldsymbol{\Sigma}_{HR} \leftarrow \min_{\Sigma} \frac{1}{2} \| \boldsymbol{S} - \boldsymbol{F}_1 \boldsymbol{\Sigma} \boldsymbol{F}_2^T \|_F^2 + \xi \| \boldsymbol{\Sigma} \|_1 \tag{24}$$

338   where $\| \cdot \|_F$ denotes the Frobenius norm, $\| \cdot \|_1$ denotes the L_1 norm, representing the sparsity of $\boldsymbol{\Sigma}$,
339   and ξ denotes the regularization parameter.
340   An effective way to solve (24) is to use the 2D fast iterative soft thresholding algorithm (FISTA)
341   [30], whose $[k+1]$-th iteration can be expressed as

342
$$\begin{cases} \boldsymbol{\Sigma}_{k+1} = \mathrm{soft}[\boldsymbol{Z}_k + \mu \boldsymbol{F}_1^H (\boldsymbol{S} - \boldsymbol{F}_1 \boldsymbol{Z}_k \boldsymbol{F}_2^T) \boldsymbol{F}_2^*, \theta] \\ \eta_{k+1} = (1 + \sqrt{1 + 4\eta_k^2})/2 \\ \boldsymbol{Z}_{k+1} = \boldsymbol{\Sigma}_{k+1} + (\eta_k - 1)(\boldsymbol{\Sigma}_{k+1} - \boldsymbol{\Sigma}_k)/\eta_{k+1} \end{cases} \tag{25}$$

343   where $\mathrm{soft}[x, \theta] = x/|x| \max(|x| - \theta, 0)$ denotes the soft thresholding function with θ as the
344   threshold, η_{k+1} denotes a variable, and $\mu \in (0, 1/\| F_1 \|_F^2 \| F_2 \|_F^2)$ denotes the step size.
345   In summary, the high-resolution imaging method based on 2D FISTA for the developed SDR
346   MF-PB-SAR system is shown in Table I.
347   Based on $\boldsymbol{\Sigma}_{LR}$ or $\boldsymbol{\Sigma}_{HR}$, the reflection coefficient of the target at (α, β) can be obtained by the
348   interpolation process, expressed as

349
$$\sigma(\alpha, \beta) = \Sigma[\alpha/(\beta_{sat} - \beta), (\alpha^2 + \beta^2)^{1/2} + \beta - \alpha^2/(\beta_{sat} - \beta)/2] \tag{26}$$

350 which forms the imaging method on the α-o-β plane.

351 At last, in order to achieve the target image on the x-o-y plane, the following approximated
352 relationships of (x, y) and (α, β) are applied in this study

$$\alpha = y, \quad \tau_{sat}^{z}(\alpha, \beta) + \tau_{sur}(\alpha, \beta) = \tau_{sat}^{z}(x, y) + \tau_{sur}(x, y) \tag{27}$$

354 where the superscript 'z' denotes that the satellite is at the position with $\alpha_{sat} = y_{sat} = 0$, based on
355 which the second equation in (27) can be simplified to

$$\sqrt{y^2 + (H/\sin\varphi + \beta)^2} + \sqrt{y^2 + \beta^2} = \sqrt{(H\cot\varphi + x)^2 + y^2 + H^2} + \sqrt{x^2 + y^2} \tag{28}$$

357 Therefore, given the target at (x, y) on the ground, its corresponding point (α, β) on the α-o-β plane
358 can be obtained based on the first equation in (27) and the solution of (28), providing the image on
359 the x-o-y plane achieved by interpolation according to the process in (26).

360
361 Table I. Procedure of the proposed high-resolution imaging method based on 2D FISTA

Input: S, F_1, F_2, μ, θ, the maximal iteration number K, and the stop parameter ς.

Initial: $\Sigma_0 = 0$, $Z_0 = 0$, and $\eta_0 = 1$.
for $k = 0$ **to** $K-1$ **do**
$\quad J_k = F_1^H (S - F_1 Z_k F_2^T) F_2^*$;
$\quad \Sigma_{k+1} = \text{soft}\,[Z_k + \mu J_k,\, \theta]$;
$\quad \eta_{k+1} = (1 + \sqrt{1 + 4\eta_k^2})/2$;
$\quad Z_{k+1} = \Sigma_{k+1} + (\eta_k - 1)(\Sigma_{k+1} - \Sigma_k)/\eta_{k+1}$;
$\quad$ **if** $\|\Sigma_{k+1} - \Sigma_k\|_F / \|\Sigma_k\|_F < \varsigma$ **then**
$\qquad K_0 = k + 1$;
$\qquad$ stop iteration.
$\quad$ **end if**
end for
Return: $\Sigma_{HR} = \Sigma_K$ **or** $\Sigma_{HR} = \Sigma_{K_0}$.

362

4. Experiment results

364 Thanks to the transportable capability of the developed SDR MF-PB-SAR system, various
365 experiments were conducted at different locations. In this Section, some imaging results are
366 presented to validate the system and the proposed methods.

367 The first experiment we conducted is at a mountainous area in Besançon, France, as shown in
368 Fig. 8, where the aerial picture of the scene is also shown as the reference for imaging, provided by
369 OpenStreetMap. The observation is during the ascending pass of Sentinel-1 so that the scene is
370 illuminated from the West and the surveillance antenna is oriented to the East to collect the signals
371 reflected by the targets. Here, the IW 3 signal is selected and processed, where the incident angle is
372 set as $\varphi = 47°$ and all other parameters are the same as Fig. 5 (a), i.e., $\chi = 60$, $N_r = 2401$, $P = 251$, and T
373 = 593.18 μs. It should be noted that the dataset used to draw Figs. 2, 3, and 5 are obtained by this
374 experiment.

375 The imaging results with respect to α_l and β_l obtained by 2D IFFT based method and 2D FISTA
376 based method are shown in Fig. 9 with a 40 dB dynamic range. It can be seen that both methods can
377 achieve well-focused images of the scene and display some clear features, while the sparsity-based
378 method enjoys higher imaging resolution and low sidelobe level, which is more clearly shown in Fig.
379 10. In Fig. 10, two cuts along the abscissa of Fig. 8 (a) and (b) for an ordinate with two isolated targets
380 are compared, demonstrating the sidelobe reduction and resolution improvement achieved by the
381 2D FISTA based imaging method.

382   Based on the image obtained by 2D FISTA, the MF-PB-SAR images on the α-o-β plane (the scene
383   size is included in Fig. 7 (a), hence the feasibility of signal approximations) and on *x-o-y* plane are
384   obtained by solving (26) and using the linear interpolation method, as shown in Fig. 11. It can be
385   observed that the abscissa/ordinate of Fig. 11 are magnified/minified as compared to Fig. 9 (b),
386   matching the ground scale of the actual scene. To assess the imaging performance, the obtained MF-
387   PB-SAR image on the *x-o-y* plane is overlaid above the aerial picture, as illuminated in Fig. 12, where
388   the abscissa of the obtained image is rotated to be parallel to the satellite flight path. It can be seen
389   that the obtained image matches well with the real scene: the mountains, man-made structures in the
390   rive shores (as indicated by rectangles), and cliff (as indicated by the arrow) can be identified.
391

(a)   (b)

Fig. 8. (a) Setup of the experiment conducted in Besançon, France at the Fort Chaudanne location and
(b) the aerial picture of the observed scene with the experiment site indicated by the red nail.

(a)   (b)
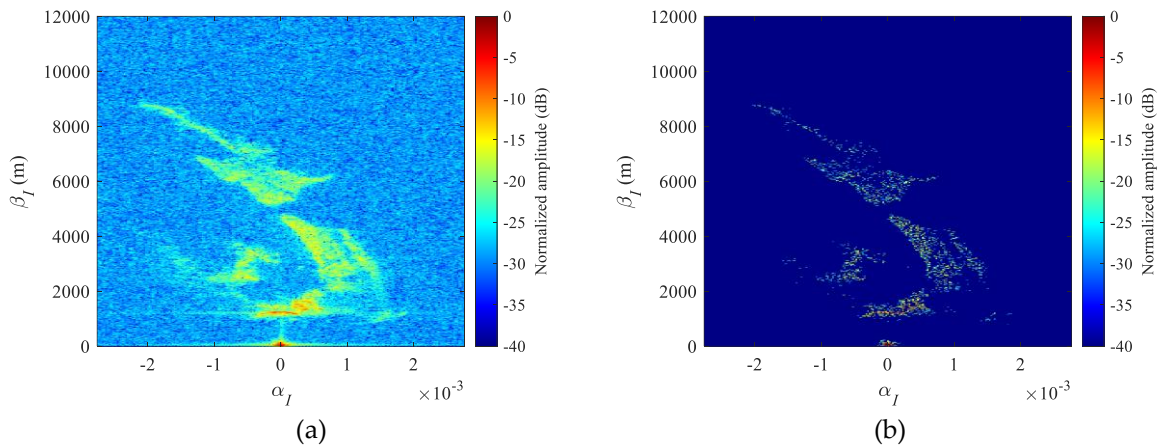
Fig. 9. Imaging results of the mountainous area in Besançon obtained by (a) 2D IFFT and (b) 2D FISTA,
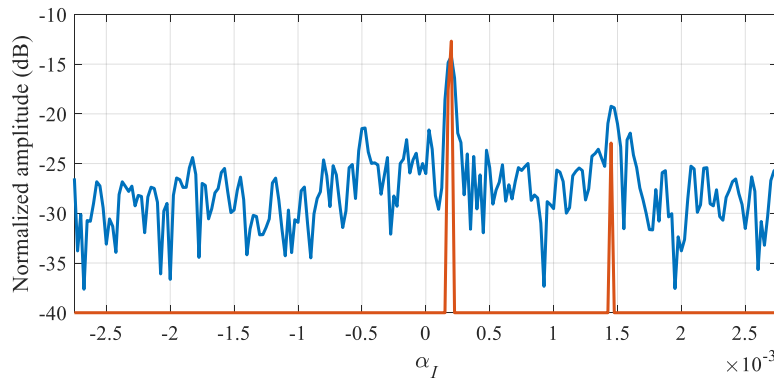the abscissa and ordinate are α_I and β_I, respectively.

Fig. 10. Sidelobe reduction and resolution improvement as observed from the cross-sections of Fig. 9
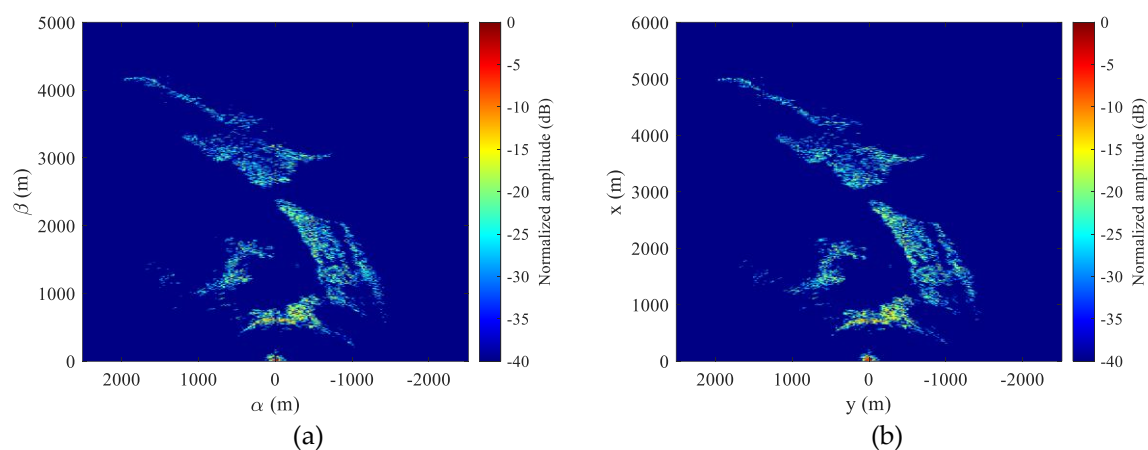(a) and (b) for an ordinate with two isolated targets.

405
406
407 Fig. 11. MF-PB-SAR images of the mountainous area in Besançon on (a) the α-o-β plane and (b) the x-
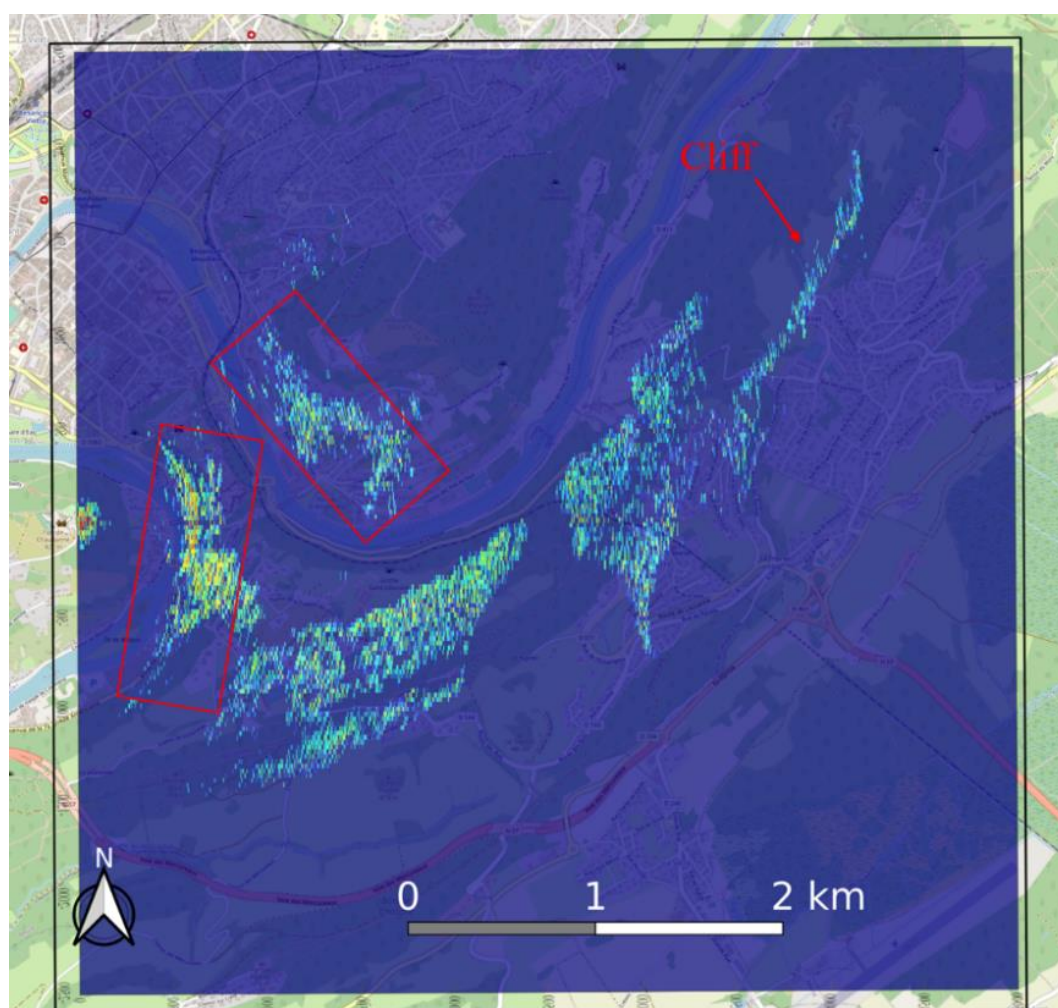408 o-y plane, obtained by the linear interpolation process.
409

410
411 Fig. 12. MF-PB-SAR image of the mountainous area in Besançon during an ascending pass with the
412 satellite beam facing East, overlaid with the aerial picture provided by OpenStreetMap.
413

414   The second experiment we conducted is at an urban area in Paris, France, as shown in Fig. 13.
415 This aera contains abundant targets, e.g., building, street, and park, for imaging and the landmark of
416 Paris, Eiffel Tower, is about 5.73 km from the experiment site, as indicated by the red star in Fig. 13
417 (b). During the measurement, the ascending pass of Sentinel-1 illuminates the city from the West, so
418 that the surveillance antenna is facing Eastward. The IW-2 signal is selected here and the processing

419   parameters are: φ = 52°, χ = 60, N_r = 2401, P = 275, and T = 688.88 μs (i.e., the IW 2 signal fragment is
420   selected in this experiment).

421   Figure 14 (a) and (b) show the imaging results obtained by 2D FISTA on the α-o-β plane (the
422   scene size is still included in Fig. 7) and the x-o-y plane, respectively. It can be seen that the images
423   are well focused and different ground features can be easily observed. By overlaying the MF-PB-SAR
424   image on the x-o-y plane with the aerial picture provided by OpenStreetMap, as shown in Fig. 15, the
425   imaging result can be verified: long street (indicated by the rectangle), tall buildings (indicated by the
426   circles), river-shore man-made structure, park (indicated by the polygon), and the Eiffel Tower match
427   well with the actual scene.

428
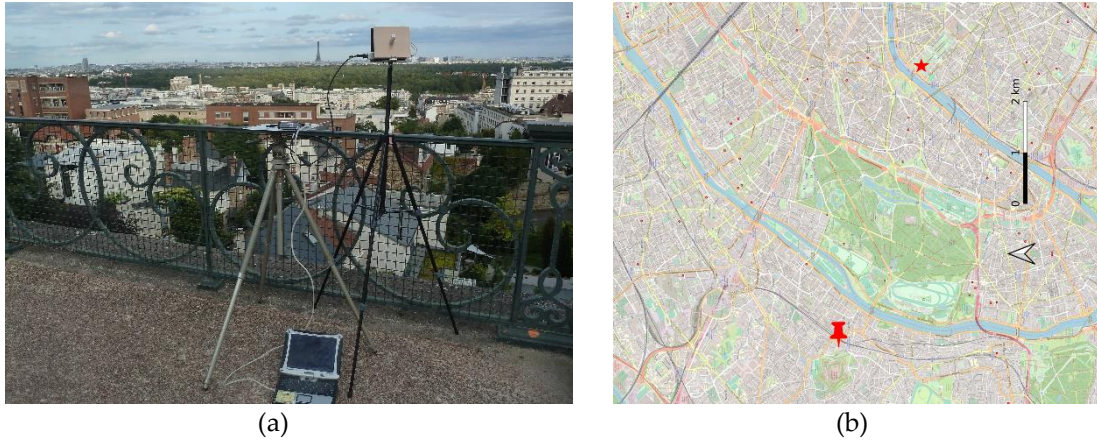
429
430   (a)   (b)
431   Fig. 13. (a) Setup of the experiment conducted in Paris, France at the Mont Valerien location and (b)
432   the aerial picture of the imaging scene, where the experiment site is indicated by the red nail.
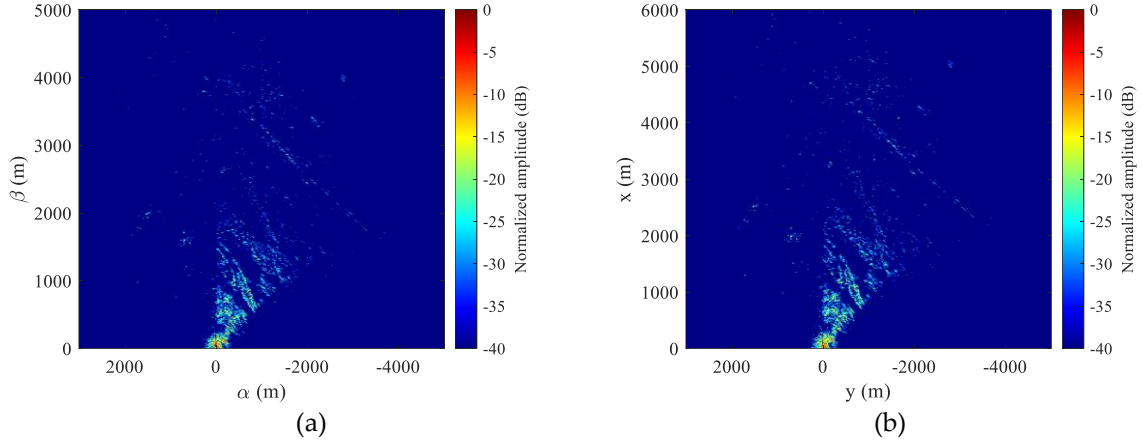
433

434
435   (a)   (b)
436   Fig. 14. MF-PB-SAR images of the urban area in Paris (a) on the α-o-β plane and (b) on the x-o-y plane,
437   obtained by the 2D FISTA based imaging method.

438

439   The third experiment we conducted is at Spitsbergen, Norway, close to the North Pole, as shown
440   in Fig. 16. Different from previous two experiments, EW illumination signal with a PRI of T = 613.25
441   μs are sampled and used for target imaging in this case. Other processing parameters are: φ = 45°, χ
442   = 60, N_r = 3201 (to achieve a longer detection range than N_r = 2401), and P = 201. Besides, to verify the
443   stability and repeatability of the developed system, two datasets were sampled with an interval of 12
444   days (i.e., the period of the satellite) at Sept. 22 and Oct. 4, 2021.
445   The imaging results at two different dates obtained by the 2D FISTA based imaging method on
446   the α-o-β plane (the scene size is still included in Fig. 7) and the x-o-y plane are shown in Fig. 17. It
447   can be seen that multiple snow mountains can be well imaged and the imaging results correspond to
448   two different dates are similar to each other, demonstrating the stability of the developed system. Fig.
449   18 shows the overlay between the MF-PB-SAR image (colorful) and the SAR image (grey) generated
450   by Sentinel1 during a pass at Oct. 3. It can be learned that the match is reasonable and the obtained

451 image can show different scattering properties of the mountains from a bistatic angle. It should be
452 mentioned that, although the measurements at two different dates allow for phase comparison in the
453 context of differential interferometry analysis, detailed analysis is ongoing.
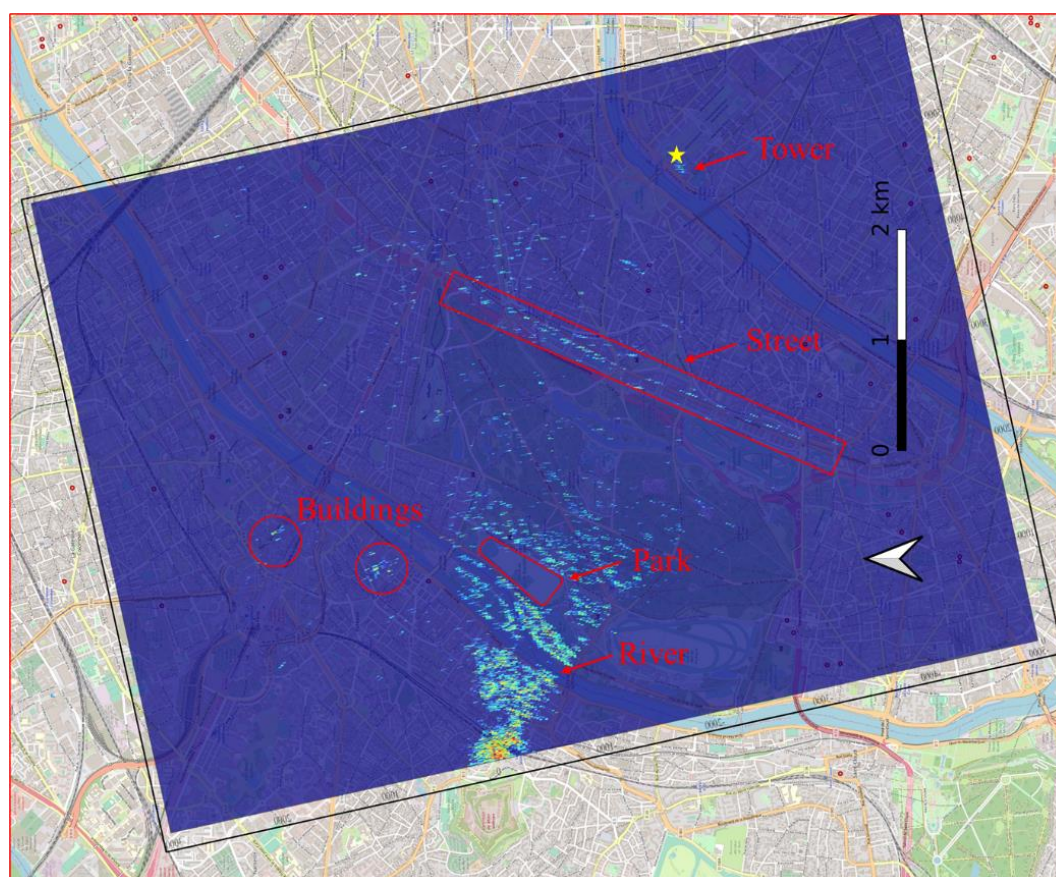454

455
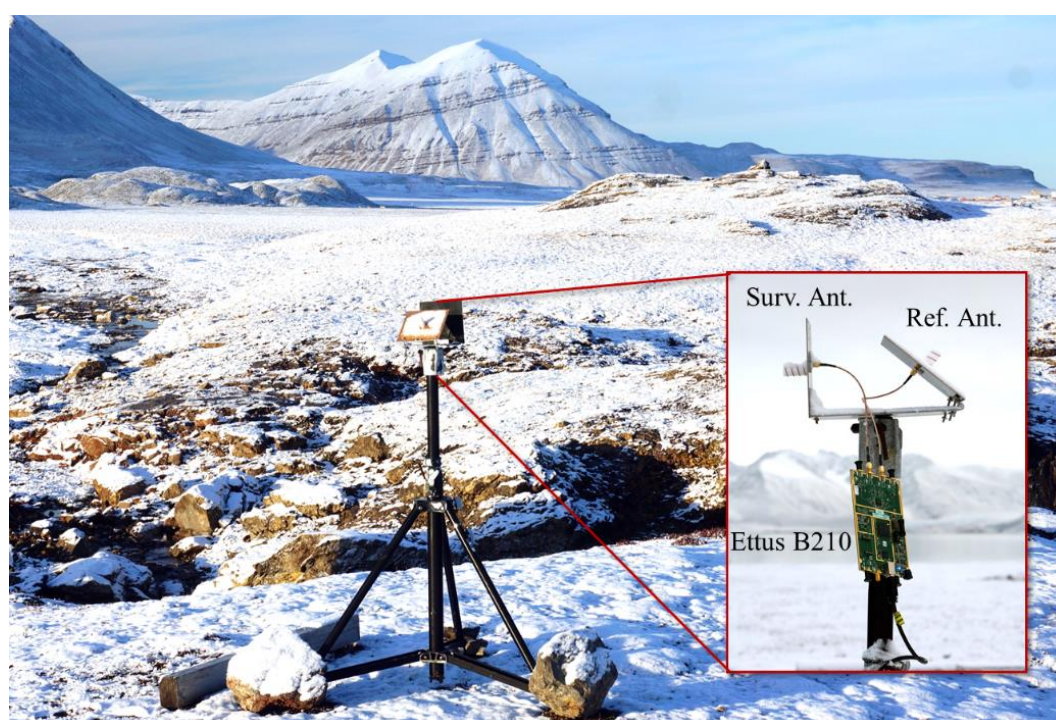456 Fig. 15. MF-PB-SAR image of the urban area in Paris, overlaid with the aerial picture.
457

458
459 Fig. 16.   Setup of the experiment conducted in Spitsbergen, Norway. The system is fixed on the same
460 position for a period of 12 days to show its stability and repeatability.
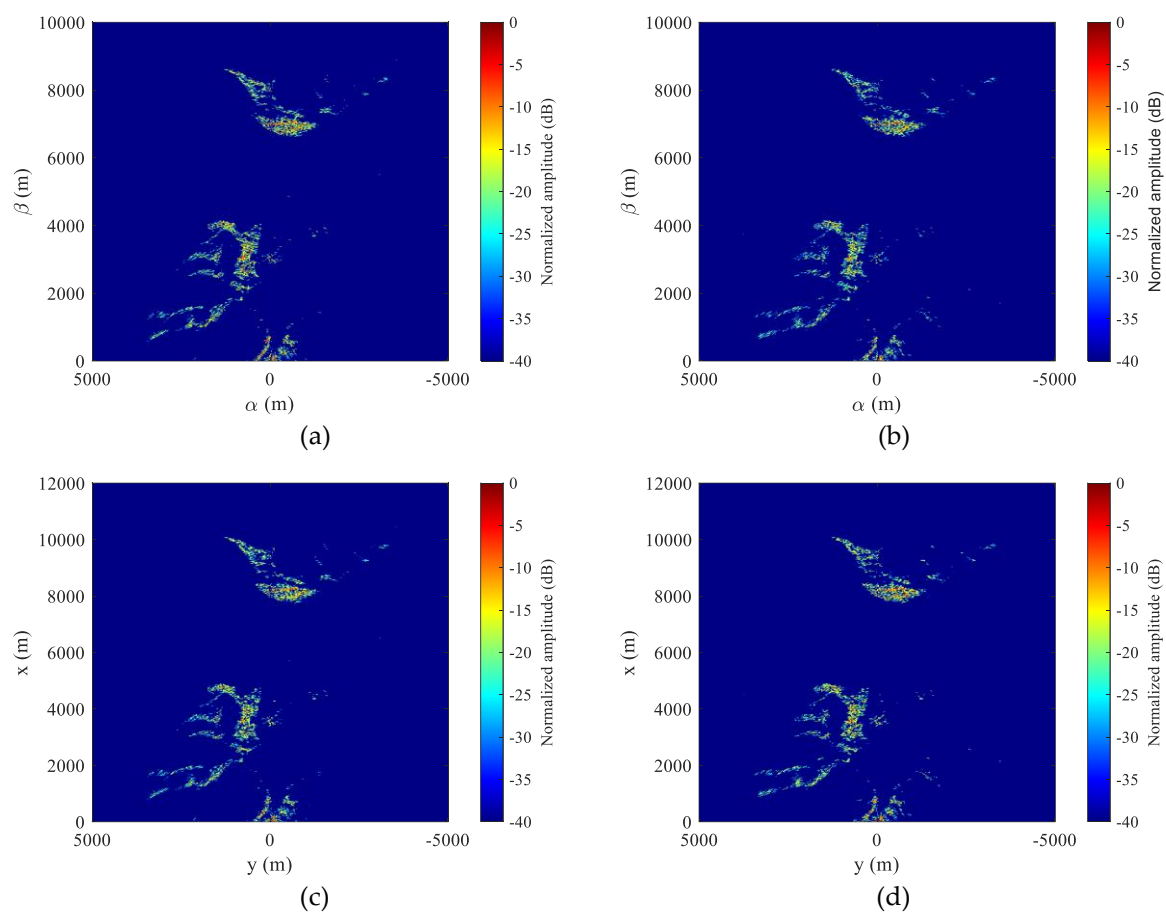
Fig. 17. MF-PB-SAR images of the snow mountains in Spitsbergen (a-b) on the α-o-β plane and (c-d) on the x-o-y plane. The left sub-figures and right sub-figures correspond to the data sampled in Sept. 22 and Oct. 4, respectively.
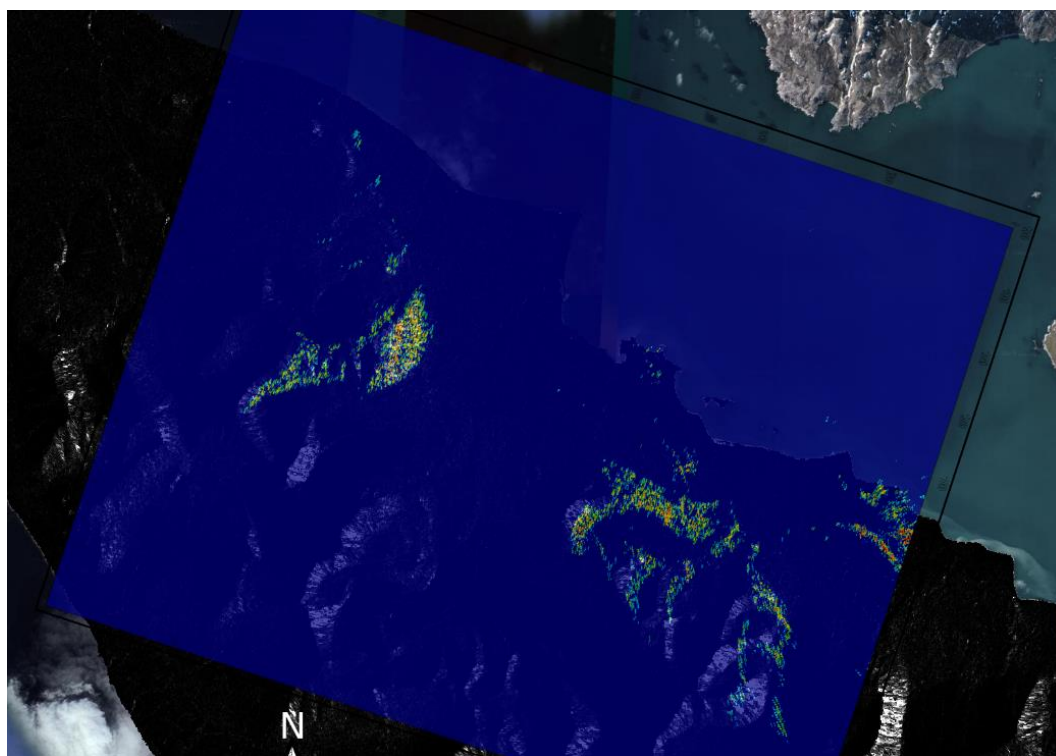

Fig. 18. Overlay between the MF-PB-SAR image obtained in Spitsbergen and the SAR image generated by Sentinel-1.

5. Conclusions

By using commercial-off-the-shelf software defined radio hardware, a passive bistatic synthetic aperture radar using the C-band SAR satellite, Sentinel-1, as its emitting source has been developed and validated, with no need for accurate time and position synchronization between the satellite in space and the fixed receiver on the ground. Its system structure, signal model, imaging geometry, signal pre-processing method, and approximation based effective target imaging methods have been introduced in this paper. Experiments in mountainous and urban aeras have been conducted and the imaging results shown that the developed system and the proposed methods can get well-focused images that match the actual local scene in a range of several kilometers. Running the full data acquisition on a Raspberry Pi 4 single board computer makes the system deployable for autonomous remote sensing measurements. Data acquisition and processing software is available at https://github.com/jmfriedt/sentinel1_pbr. In future, high-resolution target imaging methods that combine multiple signal fragments and differential interferometry processing methods will be studied and the application of the developed MF-PB-SAR system, such as the displacement monitoring of mountains, buildings, and towers, will be carried out.

Author Contributions: J.-M. Friedt proposed the idea, conducted the experiments, analyzed the data, and helped to write the manuscript; W. Feng established the signal model, proposed the processing methods, and wrote the manuscript; P. Wan helped to write the manuscript and gave suggestions on the processing methods.

Conflicts of Interest: The authors declare no conflict of interest.

References

1. Griffiths, H.D.; Baker, C.J. An Introduction to Passive Radar. Norwood, MA, USA: Artech House, 2017.
2. Huang, C.; Li, Z.; Lou, M.; Qiu, X.; An, H.; Wu, J.; Yang, J.; Huang, W. BeiDou-Based Passive Radar Vessel Target Detection: Method and Experiment via Long-Time Optimized Integration. Remote Sens., 2021, 13, 3933. https://doi.org/10.3390/rs13193933.
3. Feng, W.; Friedt, J.M.; Cherniak, G.; Sato, M. Batch Compressive Sensing for Passive Radar Range-Doppler Map Generation. IEEE Trans. Aerosp. Electron. Syst., 2019, 55(6), pp. 3090-3102.
4. Fang, Y.; Atkinson, G.; Sayin, A.; Chen, J.; Wang, P.; Antoniou, M.; Cherniakov, M. Improved Passive SAR Imaging with DVB-T Transmissions. IEEE Trans. Geosci. Remote Sens., 2020, 58, pp. 5066-5076.
5. Qiu, W.; Giusti, E.; Bacci, A.; Martorella, M.; Berizzi, F.; Zhao, H.; Fu, Q. Compressed Sensing-Based Algorithm for Passive Bistatic ISAR with DVB-T Signals. IEEE Trans. Aerosp. Electron. Syst., 2015, 51(3), pp. 2166-2180.
6. Feng, W.; Friedt, J.-M.; Nico, G.; Wang, S.; Martin, G.; Sato, M. Passive Bistatic Ground-Based Synthetic Aperture Radar: Concept, System, and Experiment Results. Remote Sens., 2019, 11, 1753. https://doi.org /10.3390 /rs11151753
7. Liu, F.; Antoniou, M.; Zeng, Z.; Cherniakov, M. Coherent Change Detection using Passive GNSS-Based BSAR: Experimental Proof of Concept. IEEE Trans. Geosci. Remote Sens., 2013, 51(8), pp. 4544–4555.
8. Feng, W.; Friedt, J.M.; Cherniak, G.; Sato, M. Passive Radar Imaging by Filling Gaps Between ISDB Digital TV Channels. IEEE J. Sel. Topics Appl. Earth Observ. Remote Sens., 2019, 12(7), pp. 2055-2068.
9. Gromek, D.; Kulpa, K.; Samczyński, P. Experimental Results of Passive SAR Imaging using DVB-T Illuminators of Opportunity. IEEE Geosci. Remote Sens. Lett., 2016, 13(8), pp. 1124-1128.
10. Gromek, D.; Radecki, K.; Drozdowicz, J.; Samczyński, P.; Szabatin, J. Passive SAR Imaging using DVB-T Illumination for Airborne Applications. IET Radar, Sonar & Navigation, 2019, 13(2), pp. 213-221.

11. Feng, W.; Friedt, J.-M., Cherniak, G.; Hu, Z.; Sato, M. Direct Path Interference Suppression for Short-Range Passive Bistatic Synthetic Aperture Radar Imaging Based on Atomic Norm Minimisation and Vandermonde Decomposition. IET Radar, Sonar & Navigation, 2019, 13(7), pp. 1171-1179.

12. Krysik, P.; Maslikowski, L.; Samczynski, P.; Kurowska, A. Bistatic Ground-Based Passive SAR Imaging Using TerraSAR-X as An Illuminator of Opportunity. In Proc. IEEE International Conference on Radar, Adelaide, SA, Australia, Sept. 2013, pp. 39-42.

13. Zhang, H.; Deng, Y.; Wang, R.; Li, N.; Zhao, S.; Hong, F.; Wu, L.; Loffeld, O. Spaceborne/Stationary Bistatic SAR Imaging with TerraSAR-X as an Illuminator in Staring-Spotlight Mode. IEEE Trans. Geosci. Remote Sens., 2016, 54, pp. 5203-5216.

14. Ma, H.; Antoniou, M.; Cherniakov, M. Passive GNSS-Based SAR Resolution Improvement Using Joint Galileo E5 Signals. IEEE Geosci. Remote Sens. Lett., 2015, 12(8), pp. 1640-1644.

15. Liu, F.; Fan, X.; Zhang, T.; Liu, Q. GNSS-Based SAR Interferometry for 3-D Deformation Retrieval: Algorithms and Feasibility Study. IEEE Trans. Geosci. Remote Sens., 2018, 56(10), pp. 5736-5748.

16. Anghel, A.; Cacoveanu, R.; Datcu M. Repeat-Pass Spaceborne Transmitter-Stationary Receiver Bistatic SAR Interferometry-First Results. in Proc. IEEE Int. Geosci. Remote Sens. Symp., Valencia, Spain, Jul. 2018, pp. 3651-3654.

17. Anghel, A.; Cacoveanu, R.; Moldovan, A. S.; Rommen, B.; Datcu, M. COBIS: Opportunistic C-band bistatic SAR differential interferometry. IEEE J. Sel. Topics Appl. Earth Observ. Remote Sens., 2019, 12(10), pp. 3980-3998.

18. Rosu, F.; Anghel, A.; Cacoveanu, R.; Rommen, B.; Datcu, M. Multiaperture Focusing for Spaceborne Transmitter/Ground-Based Receiver Bistatic SAR. IEEE J. Sel. Topics Appl. Earth Observ. Remote Sens., 2020, 13, pp. 5823-5832.

19. Focsa, A.; Anghel, A.; Datcu, M. A Compressive-Sensing Approach for Opportunistic Bistatic SAR Imaging Enhancement by Harnessing Sparse Multiaperture Data. IEEE Trans. Geosci. Remote Sens., 2021. https:10.1109/TGRS.2021.3071861.

20. Meier, J.; Kelley, R.; Isom, B.M.; Yeary, M.; Palmer, R.D. Leveraging Software-Defined Radio Techniques in Multichannel Digital Weather Radar Receiver Design. IEEE Trans. Instrum. Meas., 61, pp. 1571-1582.

21. Prager, S.; Thrivikraman, T.; Haynes, M.S.; Stang, J.; Hawkins, D.; Moghaddam, M. Ultrawideband Synthesis for High-Range-Resolution Software-Defined Radar. IEEE Trans. Instrum. Meas., 2019, 69, pp. 3789-3803.

22. Feng, W.; Friedt, J.M.; Wan, P. SDR-Implemented Ground-Based Interferometric Radar for Displacement Measurement. IEEE Trans. Instrum. Meas., 2021, 70, 1-18.

23. https://www.esa.int/Applications/Observing_the_Earth/Copernicus

24. https://heavens-above.com/

25. Balanis, C.A. Antenna theory: analysis and design; John wiley & sons: 2015.

26. Fortuny-Guasch, J. A fast and Accurate Far-Field Pseudopolar Format Radar Imaging Algorithm. IEEE Trans. Geosci. Remote Sens., 2009, 47(4), pp. 1187-1196.

27. Han, K.; Wang, Y.; Chang, X.; Tan, W.; Hong, W. Generalized Pseudopolar Format Algorithm for Radar Imaging with Highly Suboptimal Aperture Length. Sci. China Inf. Sci., 2015, 58(4), pp. 1-15.

28. Bi, H.; Bi, G.; Zhang, B.; Hong, W.; Wu, Y. From Theory to Application: Real-Time Sparse SAR Imaging. IEEE Trans. Geosci. Remote Sens., 2019, 58(4), pp. 2928-2936.

29. Fang, J.; Xu, Z.; Zhang, B.; Hong, W.; Wu, Y. Fast Compressed Sensing SAR Imaging Based on Approximated Observation. IEEE J. Sel. Topics Appl. Earth Observ. Remote Sens., 2013, 7(1), pp. 352-363.

30. Li, S.; Zhao, G.; Li, H.; Ren, B.; Hu, W.; Liu, Y.; Sun, H. Near-Field Radar Imaging via Compressive Sensing. IEEE Trans. Antennas Propag., 2014, 63(2), pp. 828-833.